The Astrophysical Journal, 929:101 (10pp), 2022 April 10 https://doi.org/10.3847/1538-4357/ac5e30

Coronal Seismology Using Damping of Propagating Kink Waves

D. J. Pascoe[1], T. Van Doorsselaere[2], and I. De Moortel[1,3]
[1] School of Mathematics and Statistics, University of St. Andrews, St. Andrews, Fife, KY16 9SS, UK; david.pascoe@st-andrews.ac.uk
[2] Centre for mathematical Plasma Astrophysics, Mathematics Department, KU Leuven, Celestijnenlaan 200B bus 2400, B-3001 Leuven, Belgium
[3] Rosseland Centre for Solar Physics, University of Oslo, PO Box 1029 Blindern, NO-0315 Oslo, Norway
Received 2021 August 3; revised 2022 March 10; accepted 2022 March 14; published 2022 April 18

Abstract

We consider the use of propagating kink waves, such as those observed by the Coronal Multi-channel Polarimeter, as a diagnostic technique. The transverse structuring of the plasma may be inferred by the frequency-dependent wave damping, which is attributed to resonant absorption. We include the effect of reflection of waves at the loop footpoints, which leads to the asymmetry parameter, describing the ratio of driven wave power at the footpoints becoming weakly constrained. The classical model of resonant absorption based on an exponential damping profile significantly overestimates the damping rate in coronal loops with low density contrast ratios. The use of the exponential profile in an analysis of observations therefore leads to underestimates for the density contrast ratio and associated parameters such as the heating rate following phase mixing.

Unified Astronomy Thesaurus concepts: Magnetohydrodynamics (1964); Solar coronal seismology (1994); Solar corona (1483); Solar coronal waves (1995); Bayesian statistics (1900); Markov chain Monte Carlo (1889)

1. Introduction

Propagating transverse waves are ubiquitous in the solar atmosphere, having been detected in the corona using the Coronal Multi-channel Polarimeter (CoMP; Tomczyk et al. 2007) and in the chromosphere using Hinode (De Pontieu et al. 2007; Okamoto et al. 2007). Their strong damping in the corona was reported by Tomczyk & McIntosh (2009). The strong damping supported the interpretation of these waves as kink oscillations damped by resonant absorption. The detection of ubiquitous waves in the corona is interesting in terms of our understanding of magnetohydrodynamic (MHD) waves (e.g., Nakariakov et al. 2021), their potential contribution to coronal heating (e.g., Van Doorsselaere et al. 2020b), and the application of seismological techniques (e.g., Anfinogentov & Nakariakov 2019; Anfinogentov et al. 2022; Nakariakov et al. 2021).

Resonant absorption (Ionson 1978) had previously been used to explain the strong damping of standing kink oscillations in coronal loops (e.g., Goossens et al. 2002; Ruderman & Roberts 2002). This interpretation was applied to propagating kink waves through numerical simulations (e.g., Pascoe et al. 2010, 2011) and theoretical analysis (e.g., Terradas et al. 2010). The strong damping of propagating kink waves was measured by CoMP as a discrepancy between outward and inward wave power for a signal spatially averaged over part of a coronal loop (see Figure 1 and the top panel of Figure 3). Verth et al. (2010) demonstrated that the frequency-dependence of the ratio of powers was consistent with resonant absorption.

Numerical simulations by Pascoe et al. (2012) found that the exponential damping profile typically used to describe the attenuation of the kink mode due to resonant absorption provided a very poor description of the behavior in loops with low density contrast ratios. The simulations suggested a Gaussian damping profile instead, which was later supported by the analytical derivation by Hood et al. (2013), who specifically considered the behavior for early times and provided a relation for the Gaussian damping rate as a function of the loop transverse density profile parameters. Pascoe et al. (2013) proposed a seismological method based on measuring both the Gaussian damping behavior at early times and the exponential damping behavior at later times (see also the review by De Moortel et al. 2016). The location of the switch from Gaussian to exponential depends on the density contrast ratio and can therefore be used to estimate this parameter. The additional information provided by the shape of the damping profile addresses the problem that the damping rate alone is unable to provide unique values (e.g., Arregui & Goossens 2019) for the two unknown density profile parameters, i.e., the density contrast ratio ζ, and the inhomogeneous layer width l. The layer width is commonly normalized by the (minor) loop radius R to give $\epsilon = l/R$. The center of the inhomogeneous layer is at a radial distance $r = R$, and so limiting cases of $\epsilon = 0$ and 2 correspond to a loop with a step function density profile and a continuously varying density profile, respectively.

There is ample observational evidence for the nonexponential or Gaussian damping regime for kink oscillations (De Moortel et al. 2002; Goddard et al. 2016; Pascoe et al. 2016b; Morton & Mooroogen 2016), and it has also been shown in linear (Ruderman & Terradas 2013; Pascoe et al. 2019a) and nonlinear (Magyar & Van Doorsselaere 2016; Pagano et al. 2018; Goddard et al. 2018; Pascoe et al. 2020) numerical models of standing kink waves. Observations analyzed using both the Gaussian and exponential damping regimes have been used to perform seismological inferences of coronal loop density profiles (Pascoe et al. 2016a, 2017a, 2017c, 2018).

Pascoe et al. (2017b) estimated the width of the inhomogeneous layer using a method based on forward modeling the transverse extreme ultraviolet (EUV) profile of a coronal loop. This was applied by Goddard et al. (2017) in a statistical study of 233 loops. Pascoe et al. (2020) demonstrated that the distribution of layer widths covers the full range of $\epsilon = [0, 2]$, but favors higher values. This is consistent with the evolution of the loop density profile due to the Kelvin–

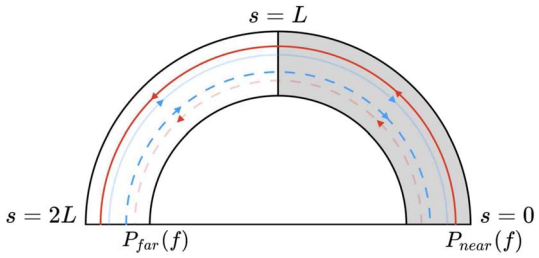

Figure 1. Data analysis method illustrated for a single reflection at the loop footpoints. The oscillation power is integrated over half the loop ($s = [0, L]$). Solid and dashed lines correspond to waves generated at the near and far footpoints, respectively. Outward-traveling waves are shown in red and inward-traveling waves in blue, with the direction defined relative to the integration region (gray).

Helmholtz instability (KHI; e.g., Terradas et al. 2008; Soler et al. 2010; Antolin et al. 2014, 2017). Analytical descriptions of resonant absorption are based on the approximation that ϵ is small. The error associated with this approximation was considered for the exponential regime by Van Doorsselaere et al. (2004) and Soler et al. (2014) and by Pascoe et al. (2019a) for the nonexponential damping regime, demonstrating that the density contrast ratio was underestimated by 50% for a typical observational case with $\epsilon \sim 1$. The numerical results from the parametric study by Pascoe et al. (2019a) are available[4] as a lookup table (LUT) that can be used, as in this paper, to generate the damping profile for some desired combination of ζ and ϵ without relying on the thin-boundary (TB) approximation. We note that this correction does not include nonlinear effects such as the KHI (e.g., Browning & Priest 1984; Ofman et al. 1994; Antolin et al. 2014). The structures generated by the KHI can increase the damping rate due to resonant absorption (Pascoe et al. 2020), which has been detected in an observation of a loop perturbed by two separate flaring releases (Pascoe et al. 2020a). Nonlinear damping can persist in the limit $\zeta \to 1$ in the case of standing waves (Van Doorsselaere et al. 2021), but not for the propagating waves (Van Doorsselaere et al. 2020a) considered in this paper. We also do not consider additional model details such as magnetic twist (e.g., Giagkiozis et al. 2016), stratification (e.g., Arregui et al. 2005; Soler et al. 2011; Ruderman et al. 2019), or flows (e.g., Bahari et al. 2020), which can also affect the damping rate.

Pascoe et al. (2015) demonstrated that a Gaussian damping profile is able to account for the CoMP power ratios analyzed by Verth et al. (2010) because the same frequency-dependent behavior is present. The data analysis is based on integrating the wave signal over half of the loop, and consequently, spatial information is lost and the exponential and Gaussian damping profiles cannot be directly distinguished in these particular observations. Pascoe et al. (2015) proposed a method using a narrower, and moving, integration window. This method was able to preserve spatial information and reveal the Gaussian damping behavior in numerical simulations, but this has not been attempted so far with observational data.

The application of the exponential model of resonant absorption to loops with low density contrast introduces errors in two ways: first, lower values of the density contrast ζ require higher values of the (normalized) layer width ϵ to provide reasonable damping rates, which makes the TB approximation an invalid assumption. Second, the shape of the damping profile is poorly described by an exponential profile when ζ is small. In this paper, we extend the method of analyzing CoMP data to consider these effects. We also include the influence of reflections at the loop footpoints for the first time. In Section 2 we describe our method and apply it to the CoMP observations initially analyzed by Verth et al. (2010) and later by Montes-Solís & Arregui (2020). In Section 3 we discuss our results in the context of the observations analyzed by Tiwari et al. (2019). Conclusions are presented in Section 4.

2. CoMP Power Ratio

We start by analyzing power ratios for propagating kink waves as measured by CoMP. We consider the effect of different analytical methods, damping profiles, and the effect of footpoint reflections on the observed kink waves. First we summarize previous results based on the exponential damping profile.

2.1. Model

The analysis of CoMP data by Verth et al. (2010) was based on an exponential spatial damping profile of the form

$$A(s) = A_0 \exp(-s/L_d), \quad (1)$$

where s is the propagation distance along the loop, A_0 is the initial amplitude, and the damping length L_d is given by the thin-tube TB approximation (Terradas et al. 2010) as

$$L_d = v_{\rm ph} \xi \frac{1}{f}, \quad (2)$$

where $v_{\rm ph}$ is the phase speed of the kink wave, f is the frequency, and ξ represents the oscillation quality factor, i.e., the ratio of damping length to wavelength, due to resonant absorption. This is a constant that depends on the transverse density profile of the loop,

$$\xi = \frac{4}{\pi^2 \kappa \epsilon}, \quad (3)$$

where $\kappa = (\zeta - 1)/(\zeta + 1)$ and $\zeta = \rho_0/\rho_{\rm e}$ is the density contrast ratio. The factor $4/\pi^2$ corresponds to a linear transition between ρ_0 and $\rho_{\rm e}$ (e.g., Arregui & Goossens 2019). We consider a linear transition profile in this paper because that is also the profile available for the Gaussian and LUT damping profiles (see also further discussion of transition profiles in Section 6.2 of Pascoe et al. 2018).

The oscillation quality factor ξ depends on two density profile parameters (ζ, ϵ) that are generally unknown. For a given value of ξ, we can consider the limit of a fully inhomogeneous loop ($\epsilon = 2$) for which the density contrast ratio will be its minimum value,

$$\zeta_{\rm min} = \frac{1 + 2/(\pi^2 \xi)}{1 - 2/(\pi^2 \xi)}, \quad (4)$$

where $\zeta_{\rm min} \to 1$ from above as $\xi \to \infty$. This is equivalent to Equation (37) of Goossens et al. (2012), with the constants corresponding to the linear rather than sinusoidal transition profile. For a given damping rate, the inferred density contrast ratio varies weakly in the limit of large ϵ, such that it is typically not much larger than $\zeta_{\rm min}$ (see, e.g., the inversion

[4] lookup table and corresponding IDL code available at https://github.com/djpascoe/kinkLUT.

curves in Goossens et al. 2008). On the other hand, it is important to note that the expressions for $\zeta_{\rm min}$ for both exponential and Gaussian damping profiles are based on the TB approximation, which becomes inaccurate in this limit. The value of $\xi = 2.69$ estimated by Verth et al. (2010) corresponds to $\zeta_{\rm min} = 1.16$, while the maximum likelihood estimation (MLE) values of ξ reported in Tiwari et al. (2019) correspond to $\zeta_{\rm min} \approx 1.1$–$1.25$. Based on the correction for wide inhomogeneous layers calculated by Pascoe et al. (2019a), we can expect these to be underestimates by approximately 50%.

The observational analysis is based on integrating the oscillation power over part of the loop length. In Verth et al. (2010), the integration is assumed to be over half of the loop, while Tiwari et al. (2019) generalize the solution to an arbitrary fraction. A key feature is that the integration region is closer to one loop footpoint than the other. Consequently, even if the drivers at the two footpoints are identical, a disparity between inward- and outward-propagating waves is revealed because the inward-propagating waves must travel farther and hence are expected to undergo greater damping.

In this paper we include the reflection of waves at the footpoints, which has the effect of turning an inward-propagating wave into an outward-propagating wave, and vice versa. To clarify this effect, we denote the power spectra at the near ($s = 0$) and far ($s = 2L$) loop footpoints as $P_{\rm near}(f)$ and $P_{\rm far}(f)$, respectively. Using this notation and following Verth et al. (2010), we define the spatially averaged outward power as

$$\langle P(f)\rangle_{\rm out} = \frac{1}{L}\int_0^L P_{\rm near}(f)\exp\left(-2s/L_d(f)\right)ds, \quad (5)$$

and the corresponding inward power as

$$\langle P(f)\rangle_{\rm in} = \frac{1}{L}\int_L^{2L} P_{\rm far}(f)\exp\left(-2s/L_d(f)\right)ds. \quad (6)$$

The ratio of the powers is then defined as

$$\langle P(f)\rangle_{\rm ratio} = \frac{\langle P(f)\rangle_{\rm out}}{\langle P(f)\rangle_{\rm in}} = \frac{P_{\rm near}(f)}{P_{\rm far}(f)}\exp\left(\frac{2L}{L_d(f)}\right). \quad (7)$$

Using the notation of Montes-Solís & Arregui (2020), we define the footpoint power ratio as $R_0 = P_{\rm near}(f)/P_{\rm far}(f)$ and note that asymmetry corresponds to $R_0 \neq 1$.

If we now consider the case of a single reflection occurring at each footpoint (see Figure 1), we obtain

$$\begin{aligned}\langle P(f)\rangle_{\rm out} &= \frac{1}{L}\int_0^L P_{\rm near}(f)\exp\left(-2s/L_d(f)\right)ds \\ &\quad + R_f^2\frac{1}{L}\int_{2L}^{3L} P_{\rm far}(f)\exp\left(-2s/L_d(f)\right)ds \\ &= \frac{P_{\rm near(f)}}{\Lambda}[1-\exp(-\Lambda)] \\ &\quad + R_f^2\frac{P_{\rm far}(f)}{\Lambda}[\exp(-2\Lambda)-\exp(-3\Lambda)],\end{aligned} \quad (8)$$

where R_f is a coefficient representing the efficiency of reflection and $\Lambda = 2L/L_d(f)$. No reflection corresponds to $R_f = 0$, whereas $R_f = 1$ describes perfect reflection (without decrease in amplitude). The inward power is similarly given by

$$\begin{aligned}\langle P(f)\rangle_{\rm in} &= \frac{1}{L}\int_L^{2L} P_{\rm far}(f)\exp\left(-2s/L_d(f)\right)ds \\ &\quad + R_f^2\frac{1}{L}\int_{3L}^{4L} P_{\rm near}(f)\exp\left(-2s/L_d(f)\right)ds \\ &= \frac{P_{\rm far(f)}}{\Lambda}[\exp(-\Lambda)-\exp(-2\Lambda)] \\ &\quad + R_f^2\frac{P_{\rm near}(f)}{\Lambda}[\exp(-3\Lambda)-\exp(-4\Lambda)].\end{aligned} \quad (9)$$

Taking the ratio of powers as before will include terms for both $P_{\rm near}(f)$ and $P_{\rm far}(f)$ in the numerator and denominator. We note that if $P_{\rm near}(f) = P_{\rm far}(f)$, the additional terms do not affect the ratio, with $\langle P(f)\rangle_{\rm ratio} = \exp(2L/L_d)$ as in Equation (7). For an exponential damping profile, the effect of reflections can therefore be neglected in the limit of weak footpoint asymmetry ($R_0 \simeq 1$). However, this result does not extend to nonexponential damping profiles. For the Gaussian damping profile in particular, the ratio of values for two locations depends on their distance from the origin (footpoint) in addition to their relative separation (see also Section 3 of Pascoe et al. 2015). Figure 2 shows examples of the variation in power ratio for a single frequency for each of the three damping profiles considered in this paper. The presence of reflections affects the power ratio for the Gaussian and LUT damping profiles even in the case of weak footpoint asymmetry, whereas the power ratio for the exponential damping profile is unaffected.

We can consider the efficiency of the reflection as an additional parameter of the model with limits $R_f = [0, 1]$. In future analysis, R_f might be considered as a function of the frequency.

2.2. Least-squares Fitting

Figure 3 shows the results of analyzing the power ratio measured by CoMP using methods based on an exponential damping profile. This analysis is not based on a single reflection, as illustrated above. Instead, the calculation of reflections continues until the reflected amplitude is lower than some cutoff, here taken to be 0.1% of the initial amplitude.

We apply our models to the data using least-squares fitting using MPFIT (Markwardt 2009). Tiwari et al. (2019) show that least-squares fitting of the power ratio can bias the inferred model parameters and overestimate the quality factor ξ in comparison with values calculated using MLE. However, here our initial aim is to demonstrate the effect of including reflections and comparison with previous analysis. We fit the observational data (circles in the top panel of Figure 3) using our model to infer the free parameters R_0 and ξ for a chosen value of R_f. Solid lines correspond to model fits using unweighted data points as in Verth et al. (2010). In the limit of $R_f \to 0$, the values of $R_0 = 0.91$ and $\xi = 2.69$ found in that study are recovered. The dashed lines use normal weights with a standard deviation of 10% of the measured value as in Montes-Solís & Arregui (2020). Again, in the limit $R_f \to 0$, the values are comparable to the maximum a posteriori (MAP) estimates of $R_0 = 0.50 \pm 0.02$ and $\xi = 1.9^{+0.3}_{-0.2}$ found in that study.

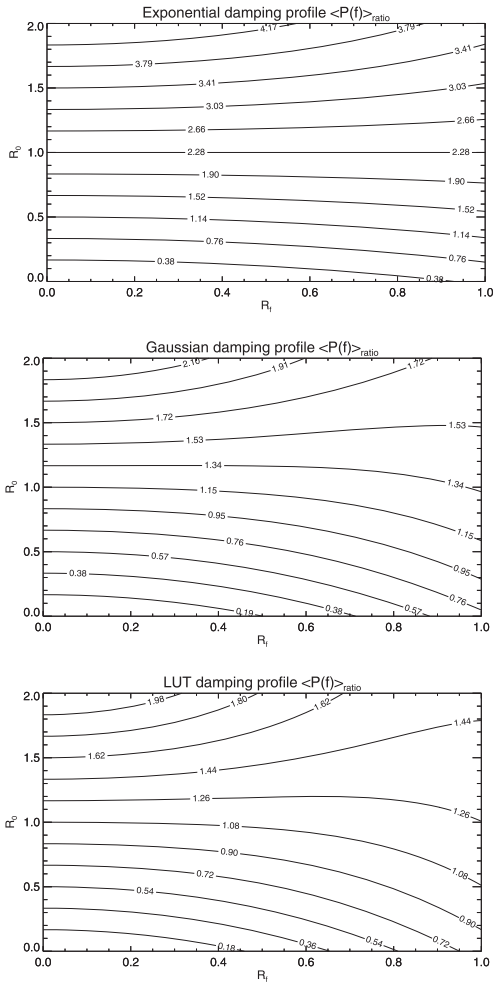

Figure 2. Variation in power ratio with the efficiency of reflection (R_f) and footpoint asymmetry (R_0) for an oscillation with frequency $f = 2$ mHz in a loop of length $2L = 500$ Mm with $v_{\rm ph} = 0.6$ Mm s^{-1} and density profile parameters $\zeta = 1.5$ and $\epsilon = 1$. The top, middle, and bottom panels correspond to the exponential, Gaussian, and LUT damping profiles, respectively.

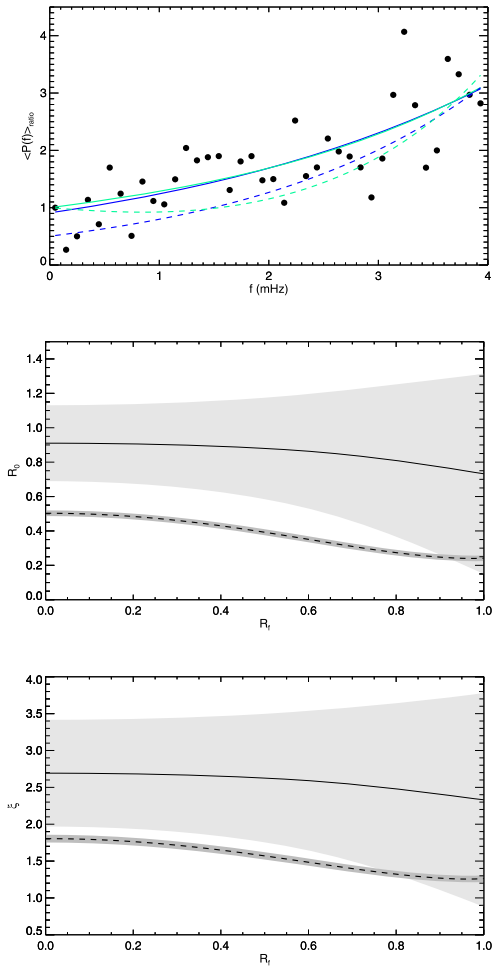

Figure 3. Analysis of the power ratio measured by CoMP based on damping due to resonant absorption with an exponential damping profile. The top panel shows the observational data (circles) with model fits for several limiting cases. Blue and green lines correspond to the limits $R_f = 0$ and $R_f = 1$, respectively. Solid lines correspond to unweighted least-squares fitting of the data points, and dashed lines show normal weighting with standard deviations assumed to be 10% of the measured value. The middle and bottom panels show the dependence of R_0 and ξ on R_f. Shaded regions correspond to the estimated errors in the fitted values.

The middle and bottom panels of Figure 3 show the fitted values of R_0 and ξ as R_f is varied from 0 to 1. For both unweighted and weighted fits, the inclusion of reflections leads to higher estimates for the footpoint asymmetry and to lower estimates for the oscillation quality factor ξ. In the case of unweighted fits, the uncertainties are large and increase with R_f such that the case of $R_0 = 1$ cannot be reliably excluded. For weighted fits, there is much less uncertainty in the model parameters, although this is based on the assumption that the observational error is lower for lower frequencies.

In the top panel of Figure 3, blue and green lines correspond to the limiting cases of $R_f = 0$ and $R_f = 1$, respectively. Due to the frequency-dependent damping rate in Equation (2), we can expect that the power ratio is insensitive to reflections for sufficiently large f because the propagating waves will already be heavily damped before they reach the other footpoint. In the limit $f \to 0$, the damping due to resonant absorption is weak and multiple reflections occur, such that inward- and outward-propagating waves are well mixed and $\langle P(f)\rangle_{\rm ratio} \to 1$. Including reflections has a larger effect on the analysis using normal weighting because the inferred footpoint asymmetry ($R_0 \neq 1$) is larger in this case, and reflections are negligible for an exponential damping profile with $R_0 \approx 1$, as discussed above. For the models with $R_f = 1$ (green lines), the power ratio $\langle P(f)\rangle_{\rm ratio} \to 1$ as $f \to 0$, whereas without reflections (blue lines), they tend to the value of the inferred footpoint asymmetry, i.e., $R_0 = 0.91$ for the unweighted fit and $R_0 = 0.50$ for normal weighting. This demonstrates that without reflections, the inferred asymmetry will be sensitive to data points in the limit $f \to 0$, whereas including reflections makes the model less sensitive to these particular points and the footpoint asymmetry will instead be inferred based on the overall properties of the data.

2.3. Bayesian Analysis

Montes-Solís & Arregui (2020) apply Bayesian analysis to the exponential damping model in Equation (7), including comparing models with and without the asymmetry parameter R_0. For the model with imposed symmetry ($R_0 \equiv 1$), the inferred oscillation quality factor is found to increase to $\xi = 4.3^{+0.7}_{-0.6}$. We perform a Bayesian analysis using the Solar

Bayesian Analysis Toolkit (SoBAT; Anfinogentov et al. 2021b). SoBAT[5] allows a wide range of data analysis problems to be investigated using Bayesian inference and Markov chain Monte Carlo (MCMC) sampling. It was initially used for the seismological analysis of kink oscillations (Pascoe et al. 2017a) and has also been applied to problems such as EUV intensity profiles (Goddard et al. 2017; Pascoe et al. 2017b), gamma-ray emission spectra (Lysenko et al. 2019), stellar superflares (Kuznetsov & Kolotkov 2021), and quasiperiodic pulsations (Broomhall et al. 2019; Pascoe et al. 2020b).

Using the same models and parameter priors as Montes-Solís & Arregui (2020), our results, based on 10^6 MCMC samples, are $R_0 = 0.50^{+0.03}_{-0.03}$ and $\xi = 1.81^{+0.61}_{-0.40}$ with footpoint asymmetry and $\xi = 4.22^{+1.57}_{-1.00}$ without footpoint asymmetry ($R_0 \equiv 1$). The uncertainties correspond to the 95% credible interval and so are larger than those in Montes-Solís & Arregui (2020), who state a 68% credible interval, but otherwise, the results are in complete agreement.

We can use Equation (3) to rewrite the model in terms of ζ and ϵ as the unknown parameters. This increase in model parameters would not permit a unique solution for methods such as least-squares fitting, but the parameter space can still be investigated using MCMC sampling. The benefit of this approach is that it is simpler to describe our prior knowledge for ζ and ϵ directly than for the combination of parameters in the definition of ξ. In particular, ϵ is defined to have limits of [0, 2]. Figure 6 of Pascoe et al. (2020) shows that there is a preference toward higher values, but this is based on the statistical study of loops observed with SDO/AIA (Goddard et al. 2017). It may be the case that these loops typically have a higher density contrast ratio than those observed with CoMP and that the bias toward larger ϵ arises due to the KHI, which is stronger for larger ζ. It is therefore reasonable to use a uniform prior with limits [0, 2] for simplicity.

The density contrast ratio must be greater than unity for an interpretation of the waves as kink oscillations damped by resonant absorption. The upper limit is more subjective, but our expectation that the density contrast ratio is low can be incorporated into the analysis. The ubiquitous waves detected by CoMP were initially interpreted as Alfvén waves in a uniform medium ($\zeta = 1$). An alternative interpretation as kink waves (Van Doorsselaere et al. 2008) is supported by their strong damping and requires $\zeta > 1$. However, the absence of bright structures in SOHO/EIT observations suggests the density contrast is not large (Tomczyk et al. 2007). Monte Carlo simulations by Morton et al. (2021) suggest that values of $\zeta = 1$–1.25 are most consistent with observations of quiescent coronal loops. Even if we assume that these are underestimates due to the TB approximation, it seems unlikely that ζ is much larger than 2.

In this paper, we use a prior based on the generalized gamma distribution. Since this distribution is defined for $x > 0$, we consider $\zeta = 1 + A$, where A is the generalized gamma distribution,

$$\mathrm{PDF}(x) = \frac{p/a^d}{\Gamma(d/p)} x^{d-1} \exp -(x/a)^p, \quad (10)$$

with shape parameters $a = 2$, $d = 1.01$, and $p = 6$, as shown in the top panel of Figure 4. These parameters give a distribution that satisfies a probability density function (PDF) ($\zeta \leqslant 1) = 0$,

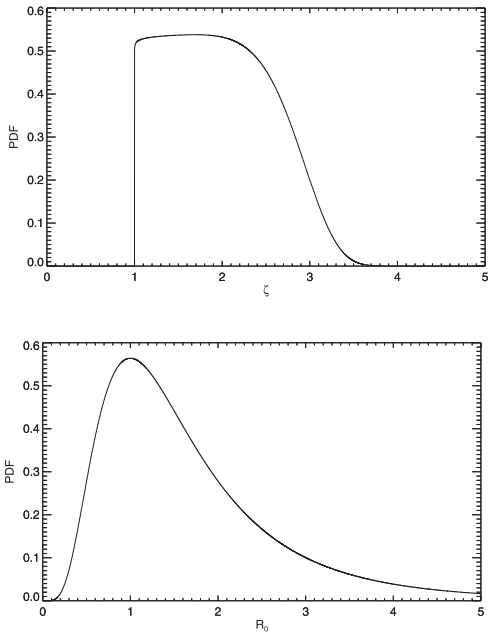

Figure 4. Prior PDFs for ζ based on a generalized gamma distribution (top panel) and for R_0 using a beta prime distribution (bottom panel).

is approximately uniform for $1 < \zeta \lesssim 2$, and then decreases rapidly such that the effective upper limit is $\zeta \approx 3.5$. In contrast, a constraint on ξ still implicitly allows values of $\zeta \to \infty$ as $\epsilon \to 0$, which are not consistent with our expectations and so need not be included in our analysis.

We also consider a different prior for R_0 than $\mathcal{U}(R_0, 0.1, 4)$ used in Montes-Solís & Arregui (2020). Since R_0 is the ratio of powers at the two footpoints and the choice of which half of the loop is analyzed is arbitrary, we expect $R_0 = x$ to have the same probability as $R_0 = 1/x$, and for $R_0 = 1$ to have the greatest probability. A convenient choice with these properties is the beta prime distribution with shape parameters $\alpha = 7$ and $\beta = 5$,

$$\mathrm{PDF}(x) = \frac{x^{\alpha-1}(1+x)^{-\alpha-\beta}}{B(\alpha, \beta)}, \quad (11)$$

where $B(\alpha, \beta)$ is the beta function. The particular choice of shape parameters is based on a mode of $(\alpha - 1)/(\beta + 1) = 1$ for which $\mathrm{PDF}(x) = \mathrm{PDF}(1/x)$, and to reflect our expectation that large asymmetries are unlikely. The uniform prior $\mathcal{U}(R_0, 0.1, 4)$ in Montes-Solís & Arregui (2020) allows power ratios of 10:1 when $P_{\mathrm{near}}(f) < P_{\mathrm{far}}(f)$ but only 4:1 when $P_{\mathrm{near}}(f) > P_{\mathrm{far}}(f)$. In that study (and our reproduction of the results discussed above), R_0 is well constrained by the data for the chosen model (exponential damping profile without reflections) and so the uniform prior did not affect the results. Our choice of a beta prime prior is therefore relevant when R_0 is not well constrained, as is the case when the effect of reflections is included.

The analyzed data being ratios of powers was also motivation for the use of the F-distribution to describe their statistical properties by Tiwari et al. (2019). We therefore also consider an F-distribution, given by Equation (18) in their study, as the likelihood ($\mathcal{L}$) function in the following Bayesian

[5] IDL code available at https://github.com/Sergey-Anfinogentov/SoBAT.

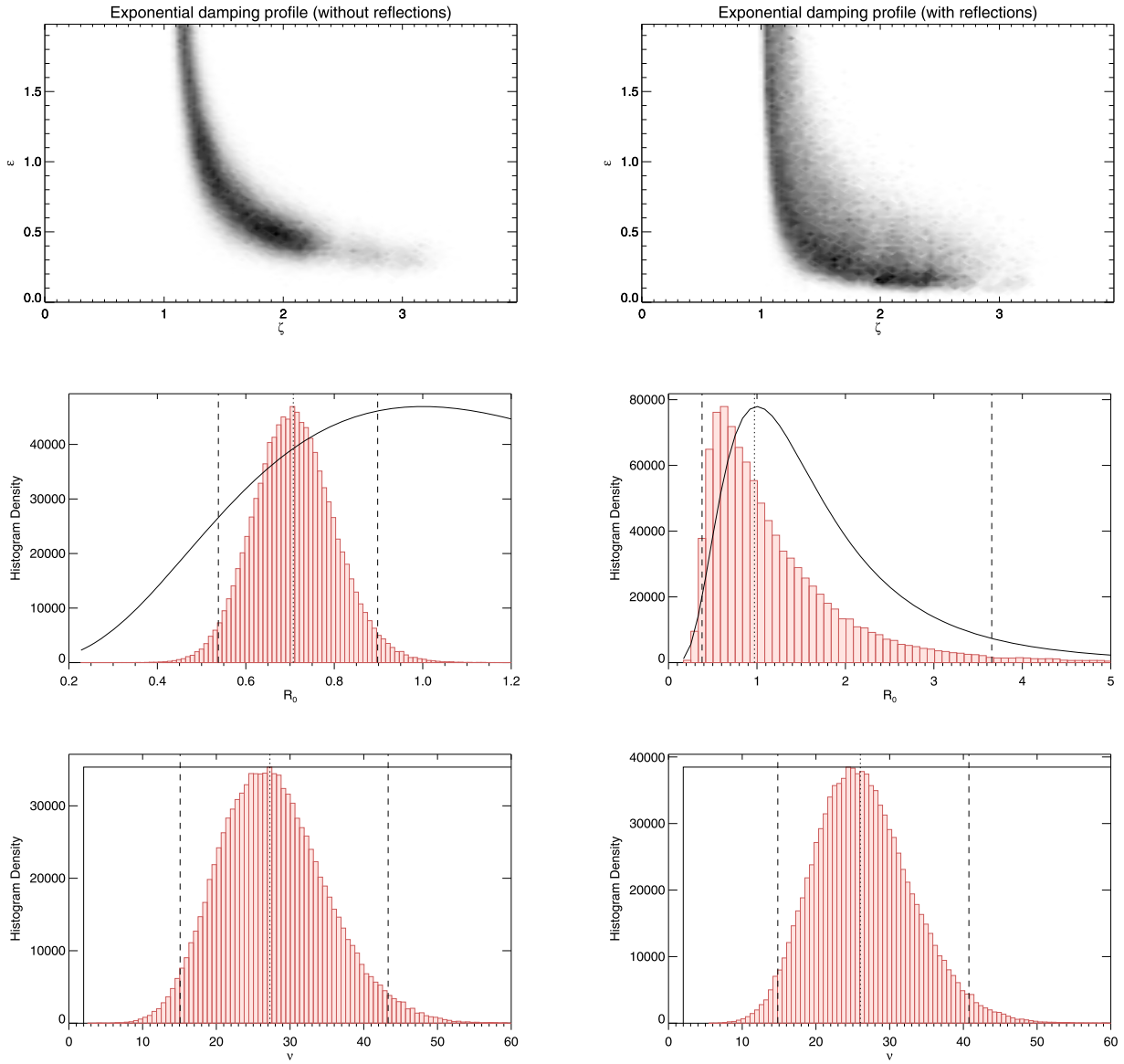

Figure 5. Bayesian analysis of the CoMP data set using an *F*-distribution likelihood function for models with an exponential damping profile without reflections (left panels) and with reflections (right panels). The panels show histograms representing the marginalized posterior probability density functions for model parameters; the density profile parameters ζ and ϵ (top), the footpoint power ratio R_0 (middle), and the degrees of freedom ν (bottom). Dotted lines denote the median values, and dashed lines show the 95% credible intervals. Solid lines are the (scaled) prior PDF.

analysis,

$$\ln \mathcal{L} = -\sum_{i=1}^{n} \ln S_i + \ln \beta(\nu/2, \nu/2) + (1 - \nu/2) \ln (R_i/S_i) + \nu \ln (1 + R_i/S_i), \quad (12)$$

where R_i are the observed and power ratios and S_i are the true values of the model. Since the number of degrees of freedom ν is unknown, we consider it as an additional free parameter of the model with the prior $\mathcal{U}(\nu, 2, 100)$. The results of this Bayesian analysis are summarized in Figure 5 for an exponential damping profile and in Figure 6 for a Gaussian damping profile. We first consider again the model for an exponential damping profile and without reflections (left panels of Figure 5). The top panels show 2D histograms approximating the marginalized posterior PDF for the loop transverse density profile parameters (ζ, ϵ). We see that ζ is being constrained by our choice of prior and that the effective maximum value defines a minimum value for ϵ. Aside from this upper limit for ζ, the posterior distribution resembles the inversion curve in Goossens et al. (2012). The asymmetry $R_0 = 0.70^{+0.20}_{-0.16}$ is weaker than that found by Montes-Solís & Arregui (2020) using relative errors of 10%, and the uncertainty is larger. We repeat our analysis with $R_0 \equiv 1$ and calculate the Bayesian evidence for our models with and without footpoint asymmetry. The Bayes factor (Jeffreys 1961; Kass & Raftery 1995) is calculated as the ratio of evidence for two models $M_{i,j}$ that describe the observational data D,

$$B_{ij} = \frac{P(D|M_i)}{P(D|M_j)}, \quad (13)$$

and

$$K_{ij} = 2 \ln B_{ij}. \quad (14)$$

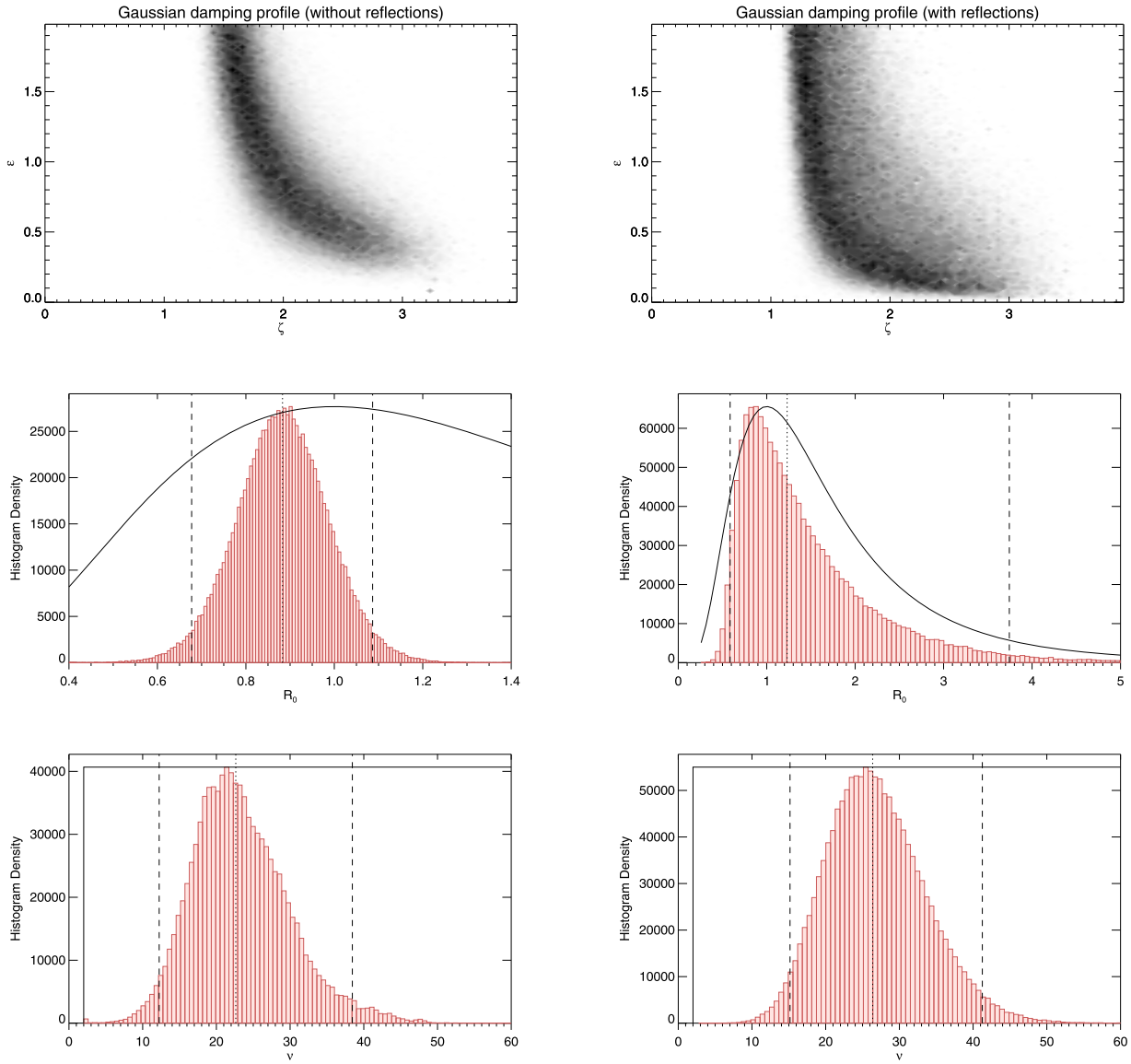

Figure 6. Same as Figure 5, but for a Gaussian damping profile.

The Bayes factor in favor of the model with asymmetry is $K = 4.3$, which is sufficient to be considered "positive" ($K > 2$) but not "strong" ($K > 6$). However, when we repeat our analysis including reflections, the Bayesian evidence for the footpoint asymmetry again becomes inconclusive. This is the case for both exponential and Gaussian damping profiles and is a consequence of a much weaker constraint on R_0. The exponential model without reflections uniquely relates R_0 to the power ratio observed in the limit $f \to 0$, as discussed earlier. The weaker constraint on R_0 also corresponds to weaker constraints on ζ and ϵ.

It would be beneficial to further constrain the model parameters using additional observational results. For example, the footpoint asymmetry might be measured directly by observations of photospheric motions (e.g., DKIST; Rast et al. 2021). The density contrast ratio may be obtained by forward modeling of EUV emission (e.g., De Moortel & Bradshaw 2008; Van Doorsselaere et al. 2016), which has been used to estimate the density and temperature contrast ratios of coronal holes (Pascoe et al. 2019b). The inhomogeneous layer width ϵ has been estimated using EUV intensity profiles (Goddard et al. 2017; Pascoe et al. 2017b), but this technique is more difficult for the case of fainter loops, especially if there are multiple overlapping structures within the observational window.

By default, SoBAT uses a likelihood function based on a multivariate normal distribution, rather than the F-distribution used here, and estimates the level of noise in the data assuming it is normally distributed. Tiwari et al. (2019) find that footpoint power ratios calculated using least-squares fitting are approximately 20%–35% higher than those using MLE analysis with an F-distribution. We find similar differences when comparing our analysis with an F-distribution likelihood function to a multivariate normal distribution. For example, with an exponential damping profile and no reflections, our inferred R_0 values are approximately 0.69 and 0.92, respectively. For our analysis using the multivariate normal distribution, the residuals (calculated using the model with MAP values for parameters) pass Kolmogorov–Smirnov, Anderson–Darling, and Lilliefors tests for normality. This indicates that a normally distributed error is capable of reproducing the behavior of this

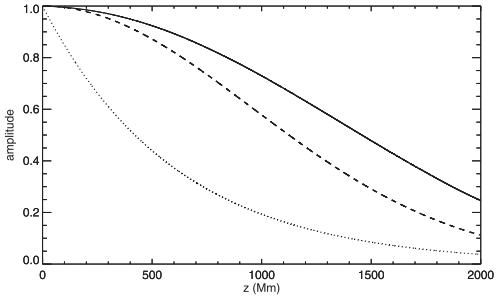

Figure 7. Exponential (dotted), Gaussian (dashed), and LUT (solid) damping profiles for $\zeta = 1.5$ and $\epsilon = 1$. The wavelength is 300 Mm, based on a frequency $f = 2$ mHz and $v_{\rm ph} = 0.6$ Mm s^{-1}.

data. However, an F-distribution is more justified based on the nature of the observational data and so allows more accurate inferences, as discussed by Tiwari et al. (2019). The F-distribution also has the benefit of potentially relating the distribution of data points with the number of structures present within the observational window, although this may be an underestimate depending on details of line-of-sight integration (e.g., De Moortel & Pascoe 2012; Karampelas et al. 2019; Pant et al. 2019). Our results (bottom panels of Figure 6) find $\nu = 26 \pm 7$, which would correspond to the spatial integration of approximately 13 pairs of input and output power spectra. This estimate, and the apparent applicability of a normal distribution, are consistent with the analysis in Appendix A of Tiwari et al. (2019), which shows the effect on the power ratios and inferred model parameters as ν increases.

3. Discussion

Accurate seismological application of propagating kink oscillations requires correction for the effect of wide inhomogeneous layers. For standing kink oscillations, this correction was calculated by Pascoe et al. (2019a). We note that this correction does not include nonlinear effects such as the KHI. However, the development of this instability depends on the density contrast ratio and our assumption of low ζ is consistent with weak KHI. The LUT damping profile can be used directly in the seismological analysis of kink waves, as demonstrated in Pascoe et al. (2019a) for a standing kink wave. However, the Gaussian damping profile provides a reasonable approximation with a much lower computational cost. Examples of the LUT, Gaussian, and exponential profiles for a coronal loop with $\zeta = 1.5$ and $\epsilon = 1$ are shown in Figure 7.

Tiwari et al. (2019) find that the rate of damping decreases for longer coronal loops, i.e., the inferred values of ξ are higher for longer loops. The range of frequencies measured by CoMP and analyzed remains the same for each loop, and so considering longer loops means that the kink waves propagate farther and damp more before they reach the other side of the loop. This is demonstrated in Figure 3 of Tiwari et al. (2019), which shows that the typical power ratio increases for longer loops as the inward waves become increasingly attenuated relative to the outward waves. Since there is typically more damping in longer loops, the effect of reflections becomes less important. Here we consider the implications of our model for this type of analysis. Figure 3 shows that not taking reflections into account causes ξ to be overestimated (assuming that reflections are actually present). The values will therefore be overestimated in general due to the assumption of the exponential damping behavior, and more so for shorter loops, for which the additional effect of reflections is greater.

To demonstrate this, we consider loops with half lengths $L = 100$–600 Mm as in Tiwari et al. (2019). For simplicity, we assume the same physical parameters for each loop and only vary the length. We take $\zeta = 1.5$ and $\epsilon = 1$, for which Equation (3) gives $\xi \approx 2.0$ (see also Figure 7). The exponential damping profile overestimates the damping rate when ϵ is large and/or ζ is small, both of which apply here, and so we expect this to be an underestimate of the actual damping that occurs. However, this value of ξ is what an analysis based on an exponential damping profile should reproduce if observations are to be used for accurate seismological diagnostics.

We assume a footpoint asymmetry of $R_0 = 0.9$. For each loop length, we generate a synthetic power ratio as a function of frequency using the LUT damping profile and including the effect of reflections ($R_f = 1$). This demonstration does not include the effect of noise in the data. We then fit the exponential model (without reflections) used in previous studies to the synthetic data. The values of ξ and R_0 inferred by unweighted least-squares fitting are shown in Figure 8. Tiwari et al. (2019) show that the use of least-squares fitting overestimates the values of ξ compared with MLE by $\sim$40%. However, in Figure 8, the overestimation compared to the known value is typically $\sim$250%, i.e., the inaccuracy associated with the exponential damping profile is far greater.

This suggests that the MLE values of ξ reported by Tiwari et al. (2019) are still overestimates and that the overestimation is larger for shorter loops. Figure 5 of Tiwari et al. (2019) shows that ξ increases with loop length, but reaches a plateau. The dependence of the overestimation on loop length suggests that this plateau may be wholly or partially a consequence of the use of the exponential damping profile in the analysis. This effect therefore potentially strengthens the observational evidence that ξ increases with length, which is interpreted as longer loops having lower density contrast ratios, for example, because a similar volume of evaporated mass is distributed along a greater length.

The bottom left panel of Figure 8 shows the estimated density contrast ratio based on Equation (3), taking $\epsilon = 1$ to be a known value. The inferred density contrast is underestimated and falls in the range 1.1–1.2, consistent with the values suggested by Morton et al. (2021).

Resonant absorption is an ideal process, but the finite inhomogeneous layer that couples kink waves to Alfvén waves also causes phase mixing of the Alfvén waves (Heyvaerts & Priest 1983) and the subsequent dissipation of wave energy (e.g., Pagano & De Moortel 2017; Pagano et al. 2018). Mann & Wright (1995) estimated the lifetime of Alfvén waves as $\tau_{\rm A} = k_{\rm a}/\omega_{\rm A}'$, where $k_{\rm a} = 1/R$ is the azimuthal wavenumber and $\omega_{\rm A}'$ is the gradient of the Alfvén frequency. Rewriting this in terms of parameters relevant to propagating waves, we obtain

$$\tau_{\rm A} = \frac{\epsilon\, v_{\rm ph}}{2\pi f} \frac{1}{(C_{\rm Ae} - C_{\rm A0})}. \quad (15)$$

This represents the timescale on which the transverse spatial scale of the propagating wave decreases due to phase mixing. The estimate of the phase mixing timescale is sensitive to the inferred density contrast ratio (e.g., Pascoe et al. 2016a), and so the value is overestimated by a factor of approximately 2–4 (as is the case for ξ).

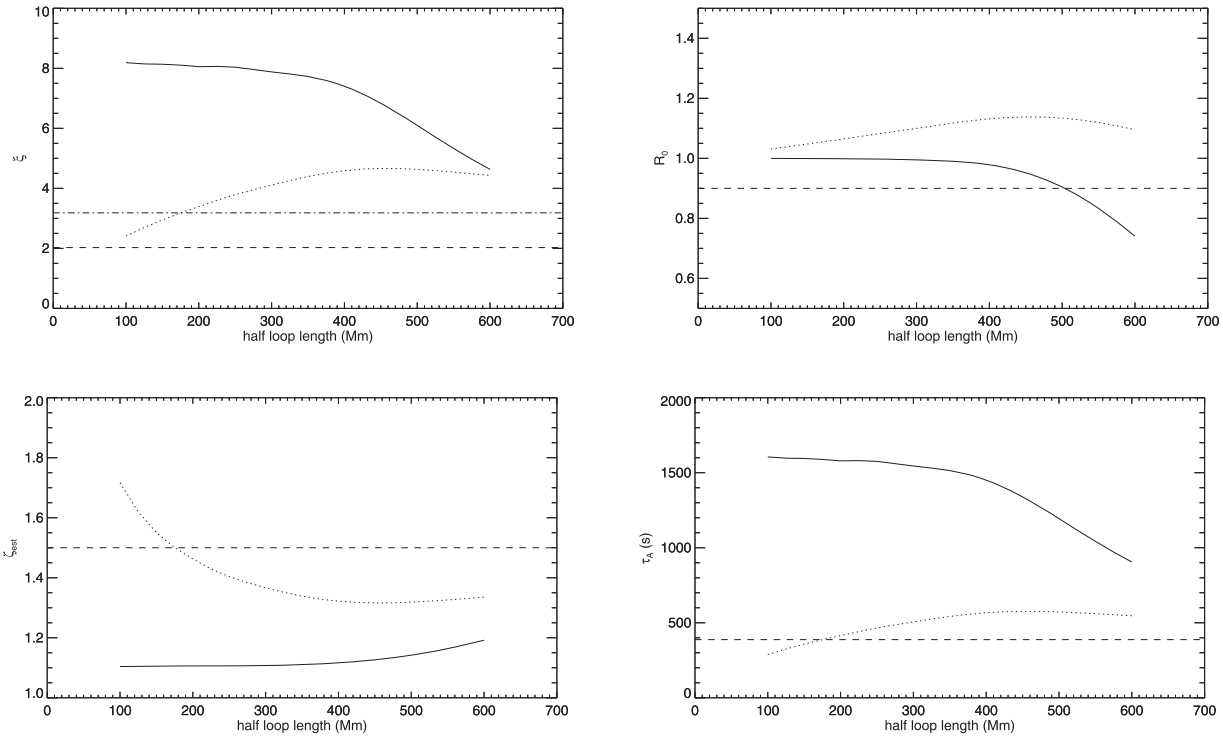

Figure 8. Estimated values of ξ and R_0 (top panels) based on an analysis of synthetic data using the exponential damping profile (without reflections). The bottom panels show the inferred values of the density contrast ratio and the phase mixing timescale (for a frequency $f = 2$ mHz). Dashed lines correspond to the true values. Dotted lines correspond to the same analysis using the Gaussian damping profile (without reflections), with the true value of ξ given by Equation (16) indicated by the dash–dotted line.

The dotted lines in Figure 8 correspond to the same analysis using the Gaussian damping profile. This is done without reflections to demonstrate the simplest but most effective improvement to the data analysis method, which only requires replacing Equations (1) and (3) with their Gaussian equivalents,

$$\begin{aligned} A(s) &= A_0 \exp\left(-s^2/2L_d^2\right), \\ \xi &= \frac{2}{\pi\kappa\sqrt{\epsilon}}. \end{aligned} \tag{16}$$

This improvement therefore comes at no additional computational cost, whereas including the effects of reflections requires some modification of the method, and the use of the LUT has a significant computational cost because it is based on numerical interpolation. We see that R_0 is overestimated by not accounting for reflections, but otherwise, there is far greater consistency between the actual and inferred values of ξ, and so the corresponding estimates for ζ and τ_A are much more accurate.

4. Conclusions

We have demonstrated an advanced method for the analysis of propagating kink waves. In particular, we combine the spatial integration method of Verth et al. (2010), the Gaussian damping profile of Pascoe et al. (2015), the statistical analysis of Tiwari et al. (2019), and a Bayesian approach as used by Montes-Solís & Arregui (2020). We showed that the MCMC method can be applied to this problem by considering the density profile parameters ζ (density contrast) and ϵ (inhomogeneous layer width) directly in order to take advantage of our greater prior knowledge for these parameters, rather than using the oscillation quality factor ξ (see Equations (3) and (16)). In this paper, our priors for ζ and ϵ describe reasonable values, but in future observational analyses, the same method could be used with stronger constraints based on additional observable properties such as the profile of the loop in EUV. We also used our MCMC method to estimate the number of loop structures within the data set based on the variations in the power ratio.

We included the additional effect of footpoint reflections for the first time and demonstrated that the footpoint asymmetry parameter becomes weakly constrained when reflections are included. Accordingly, we find no evidence against $R_0 = 1$ for this particular observation. The effect of reflections potentially strengthens the dependence of the oscillation quality factor on loop length found by Tiwari et al. (2019) because the influence of reflections on the analysis is naturally stronger for shorter loops.

The nonexponential damping profile naturally accounts for the weak damping inferred by Morton et al. (2021) and Tiwari et al. (2021) using the exponential damping profile. Since the exponential damping profile is inaccurate for loops with low density contrasts, it provides significant underestimates for the density contrast itself and for associated processes such as the heating rate due to phase mixing.

D.J.P. and T.V.D. were supported by the European Research Council (ERC) under the European Union's Horizon 2020 research and innovation program (grant agreement No. 724326) and the C1 grant TRACEspace of Internal Funds KU Leuven. The research leading to these results has received funding from the UK Science and Technology Facilities Council (consolidated grant ST/N000609/1), the European Union Horizon 2020 research and innovation program (grant agreement No. 647214). I.D.M. received funding from the Research Council of Norway through its Centres of Excellence

scheme, project number 262622. CoMP data provided courtesy of Scott W. McIntosh and Steven Tomczyk.

ORCID iDs

D. J. Pascoe https://orcid.org/0000-0002-0338-3962
T. Van Doorsselaere https://orcid.org/0000-0001-9628-4113
I. De Moortel https://orcid.org/0000-0002-1452-9330

References

Anfinogentov, S. A., Antolin, P., Inglis, A. R., et al. 2022, SSRv, 218, 9
Anfinogentov, S. A., & Nakariakov, V. M. 2019, ApJL, 884, L40
Anfinogentov, S. A., Nakariakov, V. M., Pascoe, D. J., & Goddard, C. R. 2021b, ApJS, 252, 11
Antolin, P., De Moortel, I., Van Doorsselaere, T., & Yokoyama, T. 2017, ApJ, 836, 219
Antolin, P., Yokoyama, T., & Van Doorsselaere, T. 2014, ApJL, 787, L22
Arregui, I., & Goossens, M. 2019, A&A, 622, A44
Arregui, I., Van Doorsselaere, T., Andries, J., Goossens, M., & Kimpe, D. 2005, A&A, 441, 361
Bahari, K., Petrukhin, N. S., & Ruderman, M. S. 2020, MNRAS, 496, 67
Broomhall, A.-M., Davenport, J. R. A., Hayes, L. A., et al. 2019, ApJS, 244, 44
Browning, P. K., & Priest, E. R. 1984, A&A, 131, 283
De Moortel, I., & Bradshaw, S. J. 2008, SoPh, 252, 101
De Moortel, I., Hood, A. W., & Ireland, J. 2002, A&A, 381, 311
De Moortel, I., & Pascoe, D. J. 2012, ApJ, 746, 31
De Moortel, I., Pascoe, D. J., Wright, A. N., & Hood, A. W. 2016, PPCF, 58, 014001
De Pontieu, B., McIntosh, S. W., Carlsson, M., et al. 2007, Sci, 318, 1574
Giagkiozis, I., Goossens, M., Verth, G., Fedun, V., & Van Doorsselaere, T. 2016, ApJ, 823, 71
Goddard, C. R., Antolin, P., & Pascoe, D. J. 2018, ApJ, 863, 167
Goddard, C. R., Nisticò, G., Nakariakov, V. M., & Zimovets, I. V. 2016, A&A, 585, A137
Goddard, C. R., Pascoe, D. J., Anfinogentov, S., & Nakariakov, V. M. 2017, A&A, 605, A65
Goossens, M., Andries, J., & Aschwanden, M. J. 2002, A&A, 394, L39
Goossens, M., Arregui, I., Ballester, J. L., & Wang, T. J. 2008, A&A, 484, 851
Goossens, M., Soler, R., Arregui, I., & Terradas, J. 2012, ApJ, 760, 98
Heyvaerts, J., & Priest, E. R. 1983, A&A, 117, 220
Hood, A. W., Ruderman, M., Pascoe, D. J., et al. 2013, A&A, 551, A39
Ionson, J. A. 1978, ApJ, 226, 650
Jeffreys, H. 1961, Theory of Probability (3rd edn.; Oxford: Clarendon Press)
Karampelas, K., Van Doorsselaere, T., Pascoe, D. J., Guo, M., & Antolin, P. 2019, FrASS, 6, 38
Kass, R. E., & Raftery, A. E. 1995, J. Am. Stat. Assoc., 90, 773
Kuznetsov, A. A., & Kolotkov, D. Y. 2021, ApJ, 912, 81
Lysenko, A. L., Anfinogentov, S. A., Svinkin, D. S., Frederiks, D. D., & Fleishman, G. D. 2019, ApJ, 877, 145
Magyar, N., & Van Doorsselaere, T. 2016, A&A, 595, A81
Mann, I. R., & Wright, A. N. 1995, JGR, 100, 23677
Markwardt, C. B. 2009, in ASP Conf. Ser. 411, Astronomical Data Analysis Software and Systems XVIII, ed. D. A. Bohlender, D. Durand, & P. Dowler (San Francisco, CA: ASP), 251
Montes-Solís, M., & Arregui, I. 2020, A&A, 640, L17
Morton, R. J., & Mooroogen, K. 2016, A&A, 593, A59
Morton, R. J., Tiwari, A. K., Van Doorsselaere, T., & McLaughlin, J. A. 2021, ApJ, 923, 225
Nakariakov, V. M., Anfinogentov, S. A., Antolin, P., et al. 2021, SSRv, 217, 73
Ofman, L., Davila, J. M., & Steinolfson, R. S. 1994, GeoRL, 21, 2259
Okamoto, T. J., Tsuneta, S., Berger, T. E., et al. 2007, Sci, 318, 1577
Pagano, P., & De Moortel, I. 2017, A&A, 601, A107
Pagano, P., Pascoe, D. J., & De Moortel, I. 2018, A&A, 616, A125
Pant, V., Magyar, N., Van Doorsselaere, T., & Morton, R. J. 2019, ApJ, 881, 95
Pascoe, D. J., Anfinogentov, S., Nisticò, G., Goddard, C. R., & Nakariakov, V. M. 2017a, A&A, 600, A78
Pascoe, D. J., Anfinogentov, S. A., Goddard, C. R., & Nakariakov, V. M. 2018, ApJ, 860, 31
Pascoe, D. J., Goddard, C. R., Anfinogentov, S., & Nakariakov, V. M. 2017b, A&A, 600, L7
Pascoe, D. J., Goddard, C. R., Nisticò, G., Anfinogentov, S., & Nakariakov, V. M. 2016a, A&A, 589, A136
Pascoe, D. J., Goddard, C. R., Nisticò, G., Anfinogentov, S., & Nakariakov, V. M. 2016b, A&A, 585, L6
Pascoe, D. J., Goddard, C. R., & Van Doorsselaere, T. 2020, FrASS, 7, 61
Pascoe, D. J., Hood, A. W., de Moortel, I., & Wright, A. N. 2012, A&A, 539, A37
Pascoe, D. J., Hood, A. W., De Moortel, I., & Wright, A. N. 2013, A&A, 551, A40
Pascoe, D. J., Hood, A. W., & Van Doorsselaere, T. 2019a, FrASS, 6, 22
Pascoe, D. J., Russell, A. J. B., Anfinogentov, S. A., et al. 2017c, A&A, 607, A8
Pascoe, D. J., Smyrli, A., & Van Doorsselaere, T. 2019b, ApJ, 884, 43
Pascoe, D. J., Smyrli, A., & Van Doorsselaere, T. 2020a, ApJ, 898, 126
Pascoe, D. J., Smyrli, A., Van Doorsselaere, T., & Broomhall, A. M. 2020b, ApJ, 905, 70
Pascoe, D. J., Wright, A. N., & De Moortel, I. 2010, ApJ, 711, 990
Pascoe, D. J., Wright, A. N., & De Moortel, I. 2011, ApJ, 731, 73
Pascoe, D. J., Wright, A. N., De Moortel, I., & Hood, A. W. 2015, A&A, 578, A99
Rast, M. P., Bello González, N., Bellot Rubio, L., et al. 2021, SoPh, 296, 70
Ruderman, M. S., & Roberts, B. 2002, ApJ, 577, 475
Ruderman, M. S., Shukhobodskaya, D., & Shukhobodskiy, A. A. 2019, FrASS, 6, 10
Ruderman, M. S., & Terradas, J. 2013, A&A, 555, A27
Soler, R., Goossens, M., Terradas, J., & Oliver, R. 2014, ApJ, 781, 111
Soler, R., Terradas, J., Oliver, R., Ballester, J. L., & Goossens, M. 2010, ApJ, 712, 875
Soler, R., Terradas, J., Verth, G., & Goossens, M. 2011, ApJ, 736, 10
Terradas, J., Andries, J., Goossens, M., et al. 2008, ApJL, 687, L115
Terradas, J., Goossens, M., & Verth, G. 2010, A&A, 524, A23
Tiwari, A. K., Morton, R. J., & McLaughlin, J. A. 2021, ApJ, 919, 74
Tiwari, A. K., Morton, R. J., Régnier, S., & McLaughlin, J. A. 2019, ApJ, 876, 106
Tomczyk, S., & McIntosh, S. W. 2009, ApJ, 697, 1384
Tomczyk, S., McIntosh, S. W., Keil, S. L., et al. 2007, Sci, 317, 1192
Van Doorsselaere, T., Andries, J., Poedts, S., & Goossens, M. 2004, ApJ, 606, 1223
Van Doorsselaere, T., Antolin, P., Yuan, D., Reznikova, V., & Magyar, N. 2016, FrASS, 3, 4
Van Doorsselaere, T., Goossens, M., Magyar, N., Ruderman, M. S., & Ismayilli, R. 2021, ApJ, 910, 58
Van Doorsselaere, T., Li, B., Goossens, M., Hnat, B., & Magyar, N. 2020a, ApJ, 899, 100
Van Doorsselaere, T., Nakariakov, V. M., & Verwichte, E. 2008, ApJL, 676, L73
Van Doorsselaere, T., Srivastava, A. K., Antolin, P., et al. 2020b, SSRv, 216, 140
Verth, G., Terradas, J., & Goossens, M. 2010, ApJL, 718, L102